Title

High-resolution crystal structures of the photoreceptor glyceraldehyde 3-phosphate dehydrogenase (GAPDH) with three and four-bound NAD molecules.

Journal

Protein Science, 23(11)

Authors

Baker, Bo
Shi, Wuxian
Wang, Benlian
et al.

Publication Date

2014-11-01

DOI

10.1002/pro.2543

Peer reviewed

THE PROTEIN SOCIETY

High-resolution crystal structures of the photoreceptor glyceraldehyde 3-phosphate dehydrogenase (GAPDH) with three and four-bound NAD molecules

Bo Y. Baker,[1] Wuxian Shi,[2] Benlian Wang,[2] and Krzysztof Palczewski[1]*

[1]Department of Pharmacology and Cleveland Center for Membrane and Structural Biology, School of Medicine, Case Western Reserve University, Cleveland, Ohio 44106

[2]Center for Proteomics and Bioinformatics, Center for Synchrotron Biosciences, School of Medicine, Case Western Reserve University, Cleveland, Ohio 44106

Received 26 July 2014; Revised 25 August 2014; Accepted 26 August 2014
DOI: 10.1002/pro.2543
Published online 30 August 2014 proteinscience.org

Abstract: Glyceraldehyde-3-phosphate dehydrogenase (GAPDH) catalyzes the oxidative phosphorylation of D-glyceraldehyde 3-phosphate (G3P) into 1,3-diphosphoglycerate (BGP) in the presence of the NAD cofactor. GAPDH is an important drug target because of its central role in glycolysis, and nonglycolytic processes such as nuclear RNA transport, DNA replication/repair, membrane fusion and cellular apoptosis. Recent studies found that GAPDH participates in the development of diabetic retinopathy and its progression after the cessation of hyperglycemia. Here, we report two structures for native bovine photoreceptor GAPDH as a homotetramer with differing occupancy by NAD, bGAPDH(NAD)$_4$, and bGAPDH(NAD)$_3$. The bGAPDH(NAD)$_4$ was solved at 1.52 Å, the highest resolution for GAPDH. Structural comparison of the bGAPDH(NAD)$_4$ and bGAPDH(NAD)$_3$ models revealed novel details of conformational changes induced by cofactor binding, including a loop region (residues 54–56). Structure analysis of bGAPDH confirmed the importance of Phe34 in NAD binding, and demonstrated that Phe34 was stabilized in the presence of NAD but displayed greater mobility in its absence. The oxidative state of the active site Cys149 residue is regulated by NAD binding, because this residue was found oxidized in the absence of dinucleotide. The distance between Cys149 and His176 decreased upon NAD binding and Cys149 remained in a reduced state when NAD was bound. These findings provide an important structural step for understanding the mechanism of GAPDH activity in vision and its pathological role in retinopathies.

Abbreviations: APS, advanced photon source; BGP, 1,3-diphosphoglycerate; bGAPDH, bovine GAPDH; BNL, Brookhaven National Laboratory; G3P, glyceraldehyde-3-phosphate; GAPDH, glyceraldehyde 3-phosphate dehydrogenase; bGAPDH(NAD)$_3$ and bGAPDH(NAD)$_4$, bovine GAPDH with NAD bound in three or four subunits; HEPES, 2-[4-(2-hydroxyethyl)piperazin-1-yl]ethanesulfonic acid; MS, mass spectroscopy; NAD, nicotinamide adenine dinucleotide; NO, nitric oxide; NSLS, National Synchrotron Light Source; PDE6, phosphodiesterase 6; PEG, polyethylene glycol; RMSD, root-mean-square-deviation(s); ROS, rod outer segment(s); SDS-PAGE, sodium dodecyl sulfate polyacrylamide gel electrophoresis; SEC, size-exclusion chromatography.

Additional Supporting Information may be found in the online version of this article.

Disclosure: The authors declare none.

Accession numbers: The atomic coordinates have been deposited in the RCSB Protein Data Bank under accession number 4O63 for bGAPDH(NAD)$_3$ and 4O59 for bGAPDH(NAD)$_4$.

Grant sponsor: The National Eye Institute of the National Institutes of Health; Grant number: R01EY008061.

*Correspondence to: Krzysztof Palczewski; Department of Pharmacology, School of Medicine, Case Western Reserve University, 10900 Euclid Ave, Cleveland, OH 44106-4965. E-mail: kxp65@case.edu

Keywords: glyceraldehyde 3-phosphate dehydrogenase; crystal structure; structural comparison; photoreceptor; NAD; oxidization; *S*-nitrosylation; diabetic retinopathy

Introduction

Glyceraldehyde-3-phosphate dehydrogenase (GAPDH), a classic glycolytic enzyme, catalyzes the conversion of glyceraldehyde-3-phosphate (G3P) to 1,3-bisphosphoglycerate (BGP), and requires the co-factor NAD.[1] In addition to its well-known glycolytic functions, new studies have shown that mammalian GAPDH is a multifunctional protein with diverse activities[2] that play fundamental roles in a variety of pathologies, including diabetes, age-related neurodegenerative disorders, and malaria.[3] GAPDH is physiologically nitrosylated at its active Cys149 residues.[4,5] Upon *S*-nitrosylation, GAPDH serves as a NO-transferase, for example, it can bind to nuclear proteins and co-translocate to the nucleus and facilitate the degradation of nuclear proteins.[3,6,7] In the eye, the NO level is upregulated by light and decreases in the dark.[8] In cone photoreceptors, *S*-nitrosylation regulates the activity of L-type voltage-gated Ca^{2+} channels during light adaptation.[9] GAPDH is also required for heme transfer into inducible nitric oxide synthase.[10] GAPDH binding to heme is reversible and sensitive to cellular redox levels.[11] This property expands the role of GAPDH into a potential heme-sensitive chaperone in cells.

In rod outer segments (ROS) of the eye's photoreceptors, GAPDH is one of most abundant proteins, existing at levels higher than PDE6 subunits, but slightly lower than arrestin, but much higher than any other glycolytic enzyme by an order of magnitude.[12] GAPDH also participates in the development and progression of diabetic retinopathy, one of the most severe ocular complications of diabetes. The pathogenesis of diabetic retinopathy involves multiple effector pathways[13] with GAPDH considered a potential link between hyperglycemia-induced oxidative stress and major pathways implicated in the pathogenesis of diabetic complications.[14] High levels of glucose in retinas can inactivate GAPDH.[15] MS analysis indicated that the active site Cys149 was covalently modified in GAPDH from the muscle of diabetic animals.[16] Inactivation of GAPDH could result from increased mitochondrial superoxide production that in turn nitrosylates the enzyme.[17] Inactive GAPDH would divert the upstream glycolytic intermediates to alternative pathways, potentially leading to formation of advanced glycation end products that participate in the development of diabetic microvascular complications.[1,14,18]

Structures of GAPDH have been extensively studied in bacteria, archaea, and eukarya, providing detailed information on the folding, catalysis and regulation of this enzyme. The overall structure of GAPDH consists of identical subunits conserved among different species. GAPDH enzymatic activity requires the binding of NAD but the enzyme shows different binding characteristics depending on the tissue source.[19–23] Here, we present two high resolution crystal structures of GAPDH from ROS with different occupancies of NAD. These GAPDH structures provide an updated view of their NAD-binding sites, and their conformational changes induced by NAD binding.

Results

Preparation of bovine retinal GAPDH

Bovine GAPDH is loosely associated with ROS membranes.[24] In a typical preparation, we obtained about 0.2 mg of purified bGAPDH from isotonic extraction of ROS from 100 bovine retinas using NAD-agarose affinity chromatography. The purity of bGAPDH was assessed by SDS-PAGE wherein the protein exhibited a molecular weight of ~36 kDa under denaturing conditions [Fig. 1(A)]. But size exclusion chromatography analysis demonstrated that bGAPDH had a molecular weight of about 150 kDa [Fig. 1(B)]. Like other GAPDHs from various sources, bGAPDH appeared to be a tetrameric protein in solution. The catalytic activity of bGAPDH as determined for protein isolated from ROS by NAD-affinity chromatography evidenced a K_m value of 153 ± 19 μM for its G3P substrate, and a K_m value of 255 ± 23 μM for the NAD cofactor [Fig. 1(C)].

The overall structure of bGAPDH

bGAPDH readily formed crystals under several conditions (Supporting Information Fig. S1). Crystals of purified bGAPDH had NAD bound in all four subunits (bGAPDH$(NAD)_4$). Alternatively, bGAPDH could be crystallized directly from isotonic extracts of ROS (Supporting Information Fig. S1B). This extraction of native bGAPDH yielded crystals diffracting to 1.93 Å with a structure containing three subunits with NAD-bound and one subunit free of NAD (bGAPDH$(NAD)_3$). The presence of NAD further tightened the crystal packing and improved the resolution to 1.52 Å in the bGAPDH$(NAD)_4$ structure, the highest resolution for a GAPDH structure to date. Final models of bGAPDH contained 1328 protein residues (both), 304 water molecules in bGAPDH$(NAD)_3$, and 582 water molecules in bGAPDH$(NAD)_4$ (Table I). These structural models of bGAPDH showed good stereochemistry, with only Val237 appearing in disallowed regions of all four subunits.[25] However, this residue had a clear electron density in all four subunits of both bGAPDH

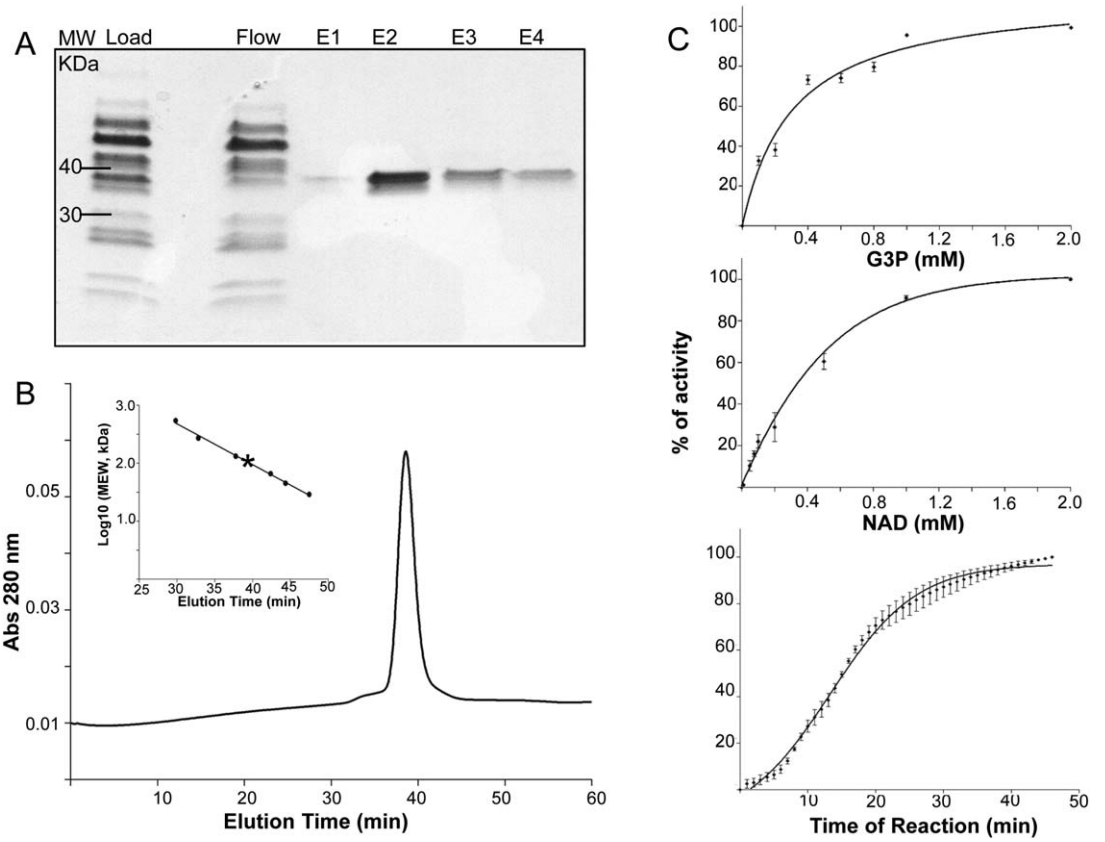

Figure 1. Characterization of bovine GAPDH. A. SDS-PAGE analysis of bGAPDH purified from bovine ROS. B. Size exclusion profile of purified bGAPDH. The column (Superdex 200, 10/300 GL, GE Healthcare) was calibrated with protein standards (Insert). C. Enzyme activity. Purified bGAPDH (0.5 μg/100 μL) was incubated with 0.2 m*M* NAD and increasing concentrations of G3P (top panel), or with 1 m*M* G3P and increasing concentrations of NAD (middle panel). After 30 min of incubation, GAPDH activity was monitored by measuring NADH production at 340 nm. Kinetic measurements were then done over a 45 min time course in the presence of 1 m*M* NAD and 1 m*M* G3P (bottom panel).

structures. The abnormal dihedral angles of this residue were also observed in other reported GAPDH structures, for example, PDB entries, 1J0X, 1U8F, and 1ZNQ. The overall folding of bGAPDH was similar to that of other previously determined eukaryotic GAPDH structures. The refined model was composed of one tetramer with four subunits shown in the typical nomenclature of GAPDH subunits' colors of green (*Q*), red (*P*), blue (*R*), and yellow (*O*) (Fig. 2).[26] The molecular axes were defined as *P*, *Q*, and *R*, and *O* subunits were related by 222 symmetry. The choice of the first monomer *O* in bGAPDH(-NAD)$_3$ was the subunit free of NAD. Each subunit was composed of a catalytic domain (residues 148–311) and a NAD-binding domain (residues 1–147 and 312–332). In the bGAPDH(NAD)$_4$ model, Ser22-Gly23-Lys24 of the *Q* subunit, and residues Gly190-Lys191 of the *O* subunit were found disordered. In the bGAPDH(NAD)$_3$ model, Gly23 (*Q, R, O*), Lys24 (*Q, O*) and Lys191 (*P, Q, O*) were disordered. Dual side-chain conformations were observed in Ser207 in subunits of *O, Q,* and *R* of the bGAPDH(NAD)$_3$ model and in Ser207 of all four subunits in the bGAPDH(NAD)$_4$ model.

bGAPDH:NAD binding

NAD was bound to bGAPDH inside a typical Rossmann-fold[27] composed of six parallel β-strands linked to two pairs of α-helices [Fig. 3(A)]. In bGAPDH(-NAD)$_4$, the presence of NAD in each subunit was clearly evidenced by a strong electron density map in the binding pocket. The averaged B-factors (Å)^2 for NAD were 12.8 (*O*), 12.7 (*P*), 12.1 (*R*), and 14.4 (*Q*). In bGAPDH(NAD)$_3$, the electron density map indicated the presence of NAD at high occupancy in subunits *P, Q*, and *R*. But no electron density was observed for NAD in subunit of *O*. Therefore, NAD was not modeled in the *O* subunit of bGAPDH(-NAD)$_3$. The averaged B-factors (Å)^2 for NAD in bGAPDH(NAD)$_3$ were 30.2 (*P*), 22.4 (*Q*), and 26.5 (*R*). Differential NAD binding to subunits of GAPDH was previously reported. For example, two NAD molecules are bound to the rabbit muscle GAPDH tetramer (PDB code: 1J0X[22]), whereas three NAD

Table I. *Data Collection, Processing and Refinement Statistics for bGAPDH with Three or Four Bound Molecules of NAD*

Data collection	Average/outer shell bGAPDH(NAD)$_3$ (Å)	Average/outer shell bGAPDH(NAD)$_4$ (Å)
Wavelength (Å)	0.9792	0.9792
Space group	$P2_1$	$P2_1$
Unit-cell parameters (Å)	$a = 79.8$, $b = 126.5$, $c = 83.8$, $\alpha = 90°$, $\beta = 118°$, $\gamma = 90°$	$a = 79.7$, $b = 125.3$, $c = 83.6$, $\alpha = 90°$, $\beta = 118°$, $\gamma = 90°$
Diffraction resolutions (Å)	50–2.0 (4.16–1.93)	50–1.52 (3.27–1.52)
No. of observations	439,689	740,361
No. of unique reflections	108,672	220,468
Redundancy	4.1 (3.9)	3.1 (3.4)
Completeness (%)	99.3 (98.4)	98.5 (96.8)
Average I/σ (I)	20.3 (2.8)	10.6 (0.9)
R_{merge} (I)	0.088 (0.56)	0.094 (0.97)
Mosaicity	0.20–0.90	0.19–0.34
Refinement		
No. of protein residues	1328	1328
No. of NAD molecules	3	4
No. of water molecules	304	582
R_{fact}	0.19	0.18
R_{free}	0.24	0.21
RMSD	0.018	0.02
Bond lengths (Å)	1.92	2.06
Bond angles (°)	0.12	0.12
Improper dihedrals (°)		
Average B factors (Å^2)	26.1	17.7
Protein	26.3	13.0
NAD^+	24.5	22.5
Water		
Ramachandran plot	95.9	96.3
(Non-Pro and Gly residues)	99.6	99.5
Favored (%)	0.36	0.45
Allowed (%)		
Disallowed (%) (Val237/*O,P,Q,* and *R*)		

molecules are bound to human placental GAPDH tetramer (PDB code: 1U8F[21]). Differential binding of NAD in GAPDH could be the basis of the cooperativity shown by this enzyme.[28–30] A diagram of the interactions between NAD and bGAPDH is shown in Figure 3(B). Details of interactions between NAD and the protein are summarized in Supporting Information Table SI.

The high quality of electron density map of bGAPDH allowed detailed modeling of solvent in its structure. Nearly a dozen water molecules were identified that interacted with NAD with a 3.2 Å cutoff inside the binding pocket (Supporting Information Fig. S2). As summarized in Supporting Information Table SII, some of these waters formed direct hydrogen bonds to NAD whereas others mediated hydrogen bonds between NAD and the protein. For example, the backbone oxygen of Glu94 formed a water-mediated (W106) interaction with the O3D of NAD. Through water-4, the O2N of NAD interacted with the backbone nitrogen groups of Gly9, Gly12 and the oxygen group of Ser95. NH1 from the side chain of Arg13 formed a water-mediated (W62) interaction with the O3B of NAD. And the ND2 side chain of Asn6 formed a water-mediated (W182) interaction with N1A of NAD.

Structural comparison of NAD-free and NAD-bound bGAPDH

The overall structures of fully NAD-bound (bGAPDH(NAD)$_4$) and partially NAD-bound (bGAPDH(NAD)$_3$) were similar. The RMSD of Cα between the two tetramers was 0.24 Å, indicating that NAD binding did not cause conformational changes in the overall folding of bGAPDH.

To study the conformational changes induced by NAD binding in bGAPDH, we performed a detailed structural comparison of the NAD-free and NAD-bound subunits. Thus the NAD-free subunit (*O*) from bGAPDH(NAD)$_3$, and the corresponding subunit *O* in bGAPDH(NAD)$_4$ (with NAD-bound) were superimposed for comparison. In addition, the NAD-free subunit (*O*) was superimposed with NAD-bound subunit (*P*) from the same bGAPDH(NAD)$_3$ tetramer structure. As controls, single NAD-binding subunits such as subunits *P* from bGAPDH(NAD)$_3$ and bGAPDH(NAD)$_4$, and subunits *O* and *P* from bGAPDH(NAD)$_4$, were superimposed and compared. Atomic distances were measured for each of the paired residues. The RMSD of the Cα atoms for each residue was plotted along with the residue number [Fig. 4(A)].

As illustrated in the plot, the catalytic domain (residues 148–311) with the exception of Gly190

This figure also includes an iMolecules 3D interactive version that can be accessed via the link at the bottom of this figure's caption.

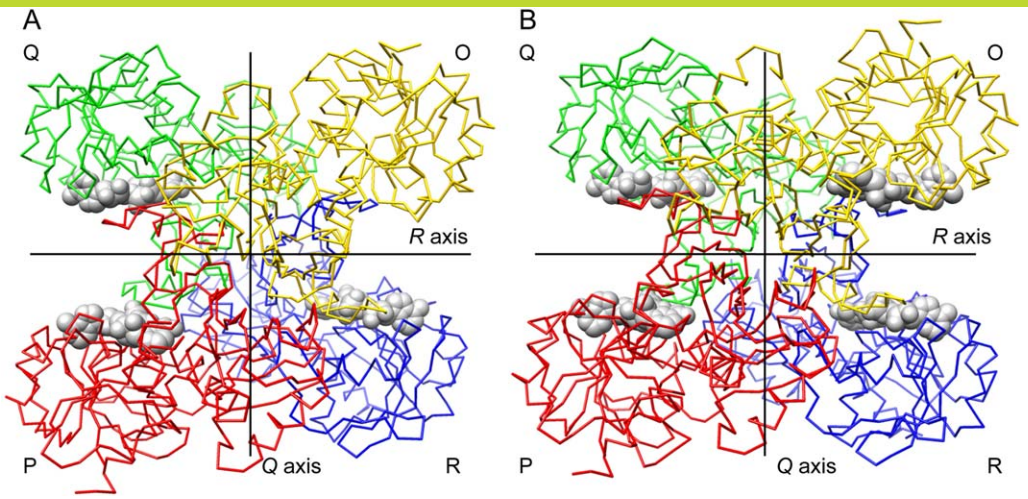

Figure 2. Carbon trace representations of bovine GAPDH tetramer structures. A. Structural model of bGAPDH(NAD)$_3$. The NAD-free subunit named as "*O*" is shown in yellow. B. Structural model of bGAPDH(NAD)$_4$. This view is down the *P* axis. Lines show the location of the *Q* and *R* twofold molecular axes. NAD cofactors are displayed in spheres. Subunit nomenclature and coloring is as described in Ref. (26). An interactive view is available in the electronic version of the article.

showed only minor fluctuations, indicating that only minor conformational changes occurred in this region. In contrast, significant peaks appeared in the NAD-binding domain. These peaks were located around residues involved in direct hydrogen bond interactions with NAD, such as Arg10, Ile11, and Asp32. Together with their neighboring residues, these regions showed substantial conformational changes upon NAD binding.

The overall RMSD value was 0.397 Å for the *O* subunits between bGAPDH(NAD)$_3$ and bGAPDH(NAD)$_4$. Some residues had much higher RMSD values than the averaged overall values. Based on the plot, the regions showing the greatest fluctuation upon NAD binding were located in the overall structure [Fig. 3(A)]. The RMSD values at Cα of the residues from these regions are presented in Supporting Information Table SIII.

Residues 54–56 evidenced large peaks in the plot [Fig. 4(A), insert]. These residues were found in the loop region shown in red in Figure 3(A). This loop is located at the surface of the tetramer structure, and is not adjacent to the NAD-binding cavity.

This figure also includes an iMolecules 3D interactive version that can be accessed via the link at the bottom of this figure's caption.

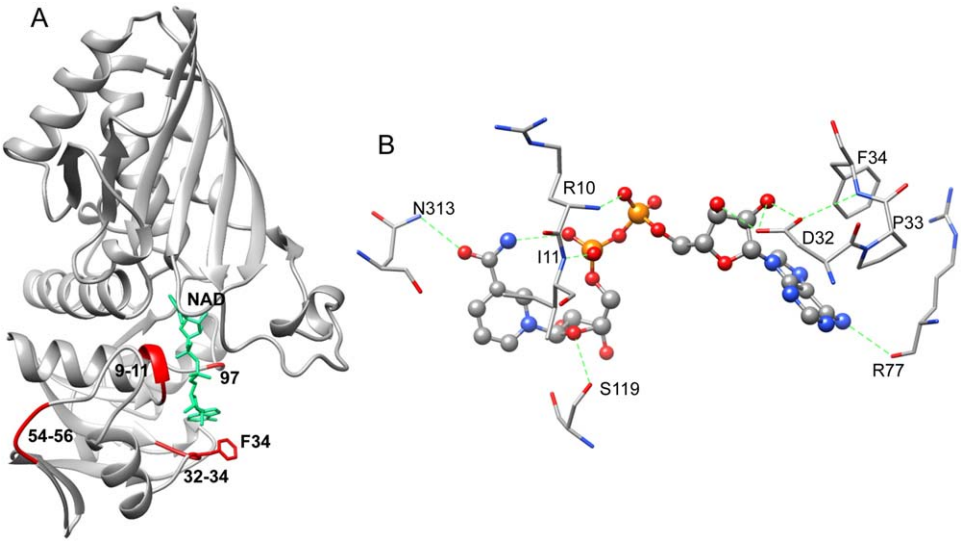

Figure 3. NAD conformation and interactions in bGAPDH. A. Ribbon presentation of NAD binding to bGAPDH(NAD)$_4$ (*P* subunit) in a typical Rossmann fold.[27] The fluctuation regions, residues 9–11 (the Gly-rich loop), 32–34 (gate for NAD entry), 54–56 (a remote loop region), and 96 are shown in red ribbons. The view of NAD binding (shown in green) and Phe34 (shown in red) in the *P* subunit of bGAPDH(NAD)$_4$ is also portrayed. B. Diagram of NAD–protein interactions in the *P* subunit of bGAPDH(NAD). Green dotted lines indicate hydrogen bonds formed between NAD and residues from the protein. An interactive view is available in the electronic version of the article.

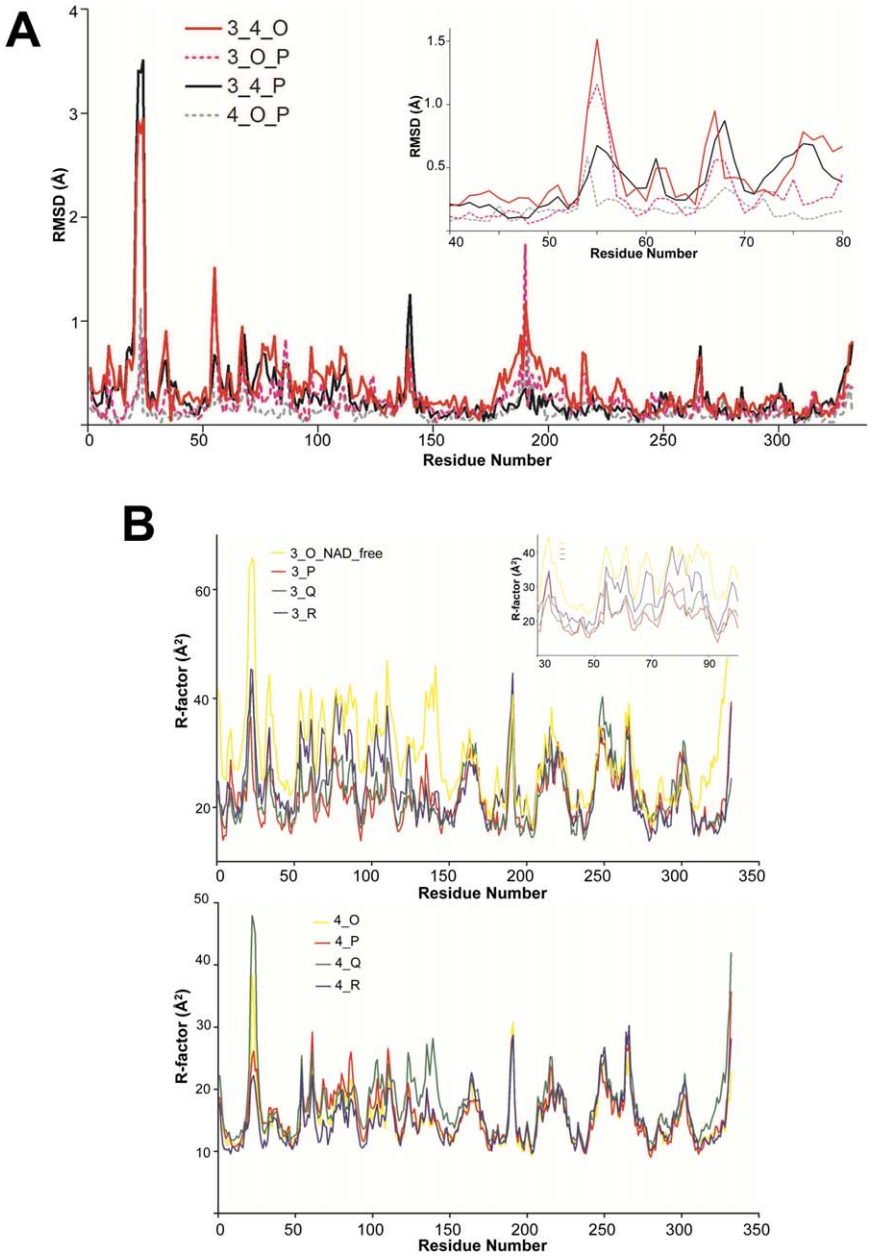

Figure 4. Structural comparison of the NAD-free and NAD-bound subunits. (A). The RMSD of Cα atoms in paired residues from apo- and holo-subunits of bGAPDH. The subunit of *O* (NAD-free) from bGAPDH(NAD)$_3$ and subunit *O* (NAD-bound) from bGAPDH(NAD)$_4$ were superimposed (solid red line, labeled as 3_4_*O*). Subunits of *O* (NAD-free) and *P* (NAD-bound) from bGAPDH(NAD)$_3$ were superimposed (dotted red line, labeled as 3_*O*_*P*). Subunits of *P* from bGAPDH(NAD)$_3$ and bGAPDH(NAD)$_4$ were superimposed as one control (solid black line, labeled as 3_4_*P*) and subunits of *O* and *P* from fully bGAPDH(NAD)$_4$ were superimposed as another control (dotted gray line, labeled as 4_*O*_*P*). Insert shows the plotted region comprised residues 40–80. B. Comparison of B-factors of residues in the main chains of apo- and holo-subunits of bGAPDH. The averaged B-factor values of the residue from main chain atoms from the four subunits of bGAPDH(NAD)$_3$ were plotted along with the residue number (upper panel, solid lines, labeled as 3_*O* (NAD_free), 3_*P*, 3_*Q*, and 3_*R*). Insert shows the plot region from residues 30 to 100. The averaged B-factor values of the residue from main chain atoms from the four subunits of bGAPDH(NAD)$_4$ were plotted along with the residue number (lower panel, solid lines, labeled as 4_*O*, 4_*P*, 4_*Q*, and 4_*R*). Each subunit was presented as a solid line colored as in Figure 2.

Flexibility of this loop may be required for adapting conformational changes upon NAD binding/release.

Furthermore, we compared the B-factor values of residues in each subunit of bGAPDH(NAD)$_3$ and bGAPDH(NAD)$_4$. The B-factor values reflect the relative flexibility of parts of a structure. Residues with low B-factors indicate a well-ordered structure, whereas residues with large B-factors indicate a flexible structure. The averaged B-factor values of Cα atoms for residues in each subunit were plotted

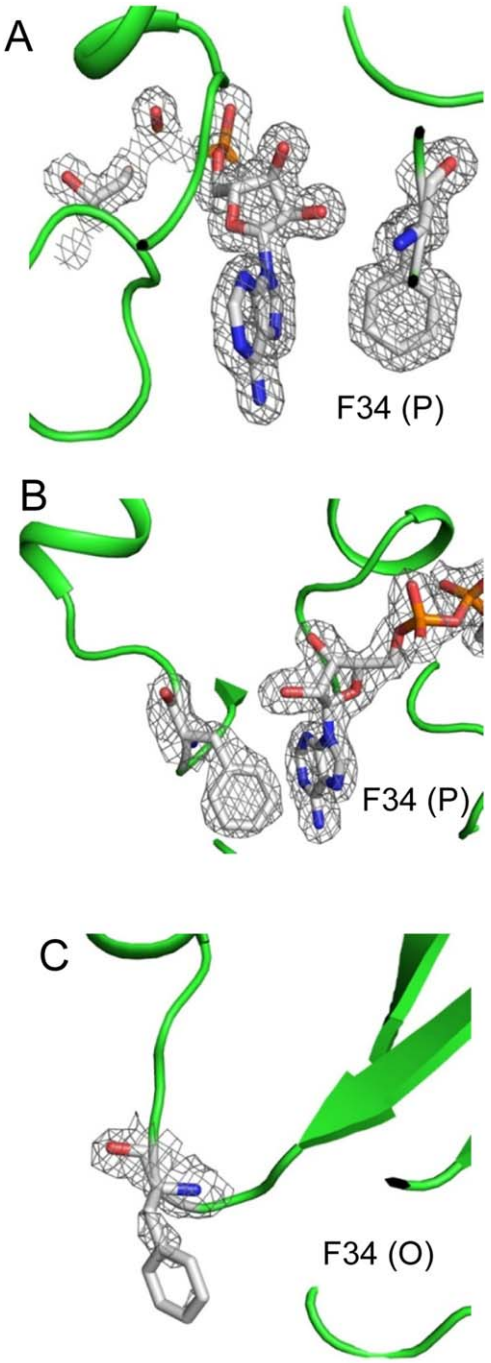

Figure 5. 2Fo–Fc maps of Phe34 in bGAPDH NAD-binding sites. The electron density was sufficient to cover the Phe34 residue and NAD molecule in the *P* subunit of both bGAPDH(NAD)$_4$ (A) and bGAPDH(NAD)$_3$ (B). But the electron density only weakly covered the main chain of Phe34 in the NAD-free structure, namely the *O* subunit of bGAPDH(NAD)$_3$ (C). 2Fo–Fc maps of Phe34 and NAD were contoured at 1.0σ and presented as gray meshes. Figures were prepared with PyMol software.

against the residues numbers [Fig. 4(B)]. In bGAPDH (NAD)$_4$, the four subunits showed only minor fluctuations in the NAD binding domain (residues 1–147), and almost identical values at the catalytic domain (residues 148–311) [Fig. 4(B), lower panel].

In contrast, the NAD-free subunit (3_*O*_NAD_-free) in bGAPDH(NAD)$_3$ had the greatest flexibility increase in the NAD binding domain, including residues 9, 34, 54, and 97. One NAD-bound subunit (3_*R*) had a mild flexibility increase and two NAD-bound subunits (3_*P* and 3_*Q*) had similar levels of flexibility [Fig. 4(B), upper panel and insert]. Nevertheless, the flexibility of the catalytic domain (residues 148–311) in bGAPDH(NAD)$_3$ remained at similar levels for all four subunits.

Residues Pro33 and Phe34 formed a bottleneck for NAD binding. Both residues showed extremely large peaks in the RMSD plot. Phe34 was located at the entry of NAD-binding pocket [Fig. 3(A)] close to the adenine group of NAD. Substitution of Phe34 with smaller side chain (e.g., Gly or Leu), or polar residue (e.g., Thr) could abolish the NAD binding affinity, or reduce the protein's catalytic efficiency.[31] This residue was suggested to be important in stabilizing NAD binding.[31] In the full NAD-bound bGAPDH structure, an electron density for the side chain of Phe34 was observed in all four subunits [Fig. 5(A), shown with *P* subunit]. In the partially NAD-bound bGAPDH structure, the electron density for the side chain of Phe34 was observed from those subunits with NAD-bound [Fig. 5(B), shown with *P* subunit]. In the absence of NAD, only a minor electron density was observed for the side chain of Phe34 [Fig. 5(C), shown with *O* subunit], indicating that this residue adopted a flexible conformation in the absence of NAD. Furthermore, Phe34 evidenced greater B-factor values in the NAD-free bGAPDH structure, as compared to much smaller B-factor values in the NAD-bound bGAPDH structure (Table II). In the NAD-bound state, the Phe34 conformation was stabilized by an interaction with NAD. In the absence of NAD, the side chain of Phe34 exhibited much greater flexibility. The dynamic character of Phe34 explains its incomplete electron density in the partial NAD bound structure, and suggests an important role for Phe34 in stabilizing NAD binding in bovine photoreceptor GAPDH.

bGAPDH:NAD binding and active site

In GAPDH, the active site Cys residue can be oxidized in response to changing environmental redox states. In the partially NAD-bound structure, the active Cys149 exhibited an oxidative state in all four subunits. The electron density clearly reinforced the positive peaks from Fo–Fc map around the thiol group of active Cys149 (*R* subunit) [Fig. 6(A)]. The active site Cys149 residues in the partially NAD-bound structure could be modeled as sulfenic acid. In contrast, the active Cys149 was in the reduced state in all four subunits of the fully NAD-bound structure [Fig. 6(B)]. No positive peak was observed from their Fo–Fc electron density maps.

Table II. *B-Factor Values (Å^2)[a] of Phe34 in Two bGAPDH Structures*

Subunits	bGAPDH(NAD)$_3$ (Å^2)	bGAPDH(NAD)$_4$ (Å^2)	Difference (Å^2)
O	45.1 (NAD free)	13.3 (+8.4)	−23.4
P	36.5	16.3 (+8.4)	−11.8
Q	28.6	16.6 (+8.4)	−3.6
R	33.0	14.6 (+8.4)	−10
Average for whole protein	26.1	17.7	−8.4

[a] The difference in overall average B-factor value was 8.4 between the two structures. To compare the B-factor values of Phe34 from the two structures, a constant value of 8.4 was added to the B-factor value for Phe34 in bGAPDH(NAD)$_3$ that had the lower B-factor value.

Cys149 and His176 had been identified as two important residues for the mechanism of GAPDH action. The adjacent His residue can lower the p*Ka* value of the active site Cys residue and make it more reactive.[32] To estimate the effect of NAD binding on the interaction between the active Cys149 and His176 [Fig. 6(C)], we measured the distance between the thiol group of active-site Cys149 and the NE2 atom of His176. The resulting values then were compared between NAD-free and NAD-bound subunits. As shown in Table III, the distance was reduced in NAD-bound subunits of two bGAPDH structures by 0.04–0.16 Å (not significant), and by 0.33 Å compared within *O* subunits which were NAD-free in bGAPDH(NAD)$_3$ and NAD-bound in bGAPDH(NAD)$_4$. Thus the residue pairs of Cys149 and His176 were brought closer together upon NAD binding. This shortened distance between Cys149 and His176 could facilitate hydride transfer from activated Cys149 towards NAD through His176.

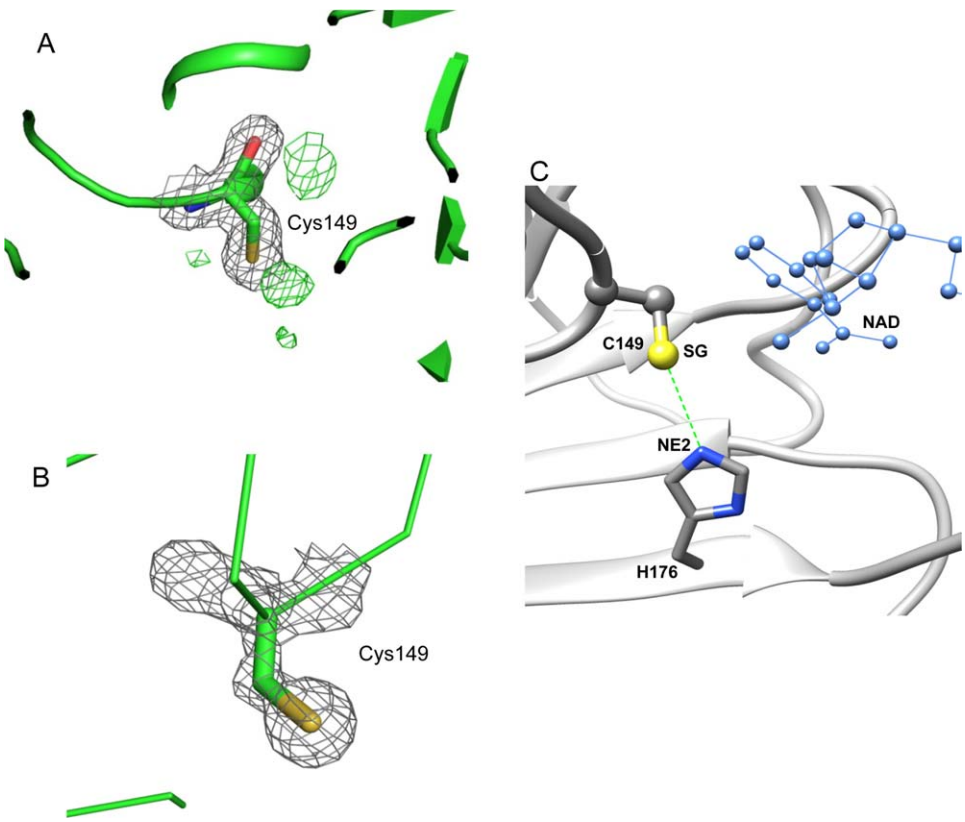

Figure 6. The active site Cys149 in bGAPDH and its interaction with His176. A. Electron density of Cys149 in subunit *R* of bGAPDH(NAD)$_3$. The 2Fo–Fc electron density map is presented as grey meshes contoured at 1.0σ. The green meshes represent a Fo–Fc electron density map contoured at 3.0σ. The presence of a positive density next to the SG atom of Cys149 strongly suggests an oxidative state for this residue. B. Electron density of Cys149 in subunit *R* of bGAPDH (NAD)$_4$. None of the four subunits exhibited a positive density next to the SG atom of Cys149 in the Fo–Fc map. Figures were prepared with PyMol software. C. Interaction between Cys149 and His176 in subunits of bGAPDH. The distance between the SG group (shown in yellow) of Cys149 and the NE2 group (shown in blue) of His176 is indicated by a dotted green line. The adjacent NAD molecule is shown in blue ball-and-sticks.

Table III. *Distance (in Å) Between SG/Cys149 and NE2/His176*

Subunits	bGAPDH(NAD)$_3$ (Å)	bGAPDH(NAD)$_4$ (Å)	Difference (Å)
O	3.75 (NAD-free)	3.42	−0.33
P	3.38	3.33	−0.05
Q	3.5	3.34	−0.16
R	3.5	3.36	−0.14

Discussion

The overall folding of GAPDH consisting of four identical subunits that form a homotetramer is conserved among different species. GAPDH enzymatic activity requires the binding of NAD but the enzyme shows different binding characteristics depending on the tissue source. Mammalian GAPDH structures display a variety of cofactor binding. In human liver (PDB entry: 1ZNQ[19]) and rat sperm (PDB entry: 2VYN[20]), the structures were fully occupied by NAD (one in each subunit). In human placenta (PDB entry: 1U8F[21]), the structure had three NADs with one subunit free of cofactor. In rabbit muscle (PDB entry: 1J0X[22]), the structure had two NADs with a single NAD molecule per dimer of the tetrameric enzyme. Whether this diversity of NAD binding resulted from the crystallization conditions is unknown. Studies of *E. coli* GAPDH[23] indicated that NAD bound to the subunits of GAPDH tetramer with different affinities, with two NAD molecules binding with a higher affinity than the remaining two.

Structures of bovine photoreceptor GAPDH retinas were determined as homotetramers with NAD partially and fully bound. The structure of bGAPDH(NAD)$_4$ in this report represents the highest resolution (1.52 Å) structure for any known GAPDH. The high quality these structural models allowed a detailed view of NAD binding in bGAPDH. Key residues and waters involving NAD binding were identified. Structural comparisons of NAD-free and NAD-bound bGAPDH models revealed regions with conformational changes upon NAD binding, including a remote loop region (residues 54–56). Structure analyses confirmed the importance of Phe34 in NAD binding in bGAPDH. Furthermore, binding of NAD in bGAPDH affected the oxidative state of the active site Cys149. With partial NAD binding, Cys149 was environmentally sensitive and found to be oxidized. With full NAD binding, the Cys149 residues were more stable and remained in a reduced state. These results indicate that NAD binding in bGAPDH plays not only a cooperative role, but also a regulatory role in catalytic activity. Together, these findings provide a structural basis for understanding the mechanism of GAPDH activity in vision and its pathological role in retinal disorders.

Materials and Methods

Data collection and processing

All crystals were soaked in their reservoir solutions with added 20% glycerol for cryoprotection. Crystals were frozen in liquid nitrogen before data collection. High resolution data sets were collected at the NSLS X29 and APS NE-CAT 24-ID-C beam lines. A 1.93 Å resolution data set was collected for crystals grown from a crude bovine ROS isotonic extract. The crystal to detector distance was 400 mm with 12% transmission. A 1.52 Å resolution data set was collected for crystals grown from purified bGAPDH in the presence of NAD. The crystal to detector distance here was 290 mm with 10% transmission. Both data sets were collected at a wavelength of 0.979 Å with an exposure time of 1 s and an oscillation range set at 1.0°.

Data were processed and scaled with HKL2000.[33] The space group for both bGAPDH crystals was $P2_1$, with a unit-cell dimension of $a = 79.8$, $b = 126.5$, and $c = 83.8$. Both data sets were virtually complete (~99%). Statistics for data collection and processing are summarized in Table I.

Structural determination and refinement

The structures of bGAPDH were solved by molecular replacement using the program Phaser[34] in the CCP4 suite.[35] The coordinates of one monomer of rabbit-muscle GAPDH (PDB code: 1J0X[22]) without ligand and water were used to search the initial model. Sequence identity between bovine and rabbit GAPDH is 98%. Model building calculations employed the diffraction data space group of $P2_1$ with components in the crystal asymmetric unit. The structural model of native bGAPDH indicated the presence of three NAD moieties with one subunit free of the cofactor. This model form was named bGAPDH(NAD)$_3$. In contrast, the structural model of purified bGAPDH displayed one NAD in each subunit. This model was designated as bGAPDH(NAD)$_4$. Both models were refined with Refmac5[36] at 10 cycles using automatic weighting with experimental sigma to obtain the X-ray terms. Protein sequence fitting and manual model adjustments were performed with Coot.[37] Based on electron density maps, the geometry of backbone and rotamers of residue side chains were justified, followed by refinement with Refmac5. The final R-factor and R-free values for bGAPDH(NAD)$_3$ were 0.19 and 0.23 at 1.93 Å resolution, and 0.18 and 0.21 for bGAPDH(NAD)$_4$ at the same resolution, respectively.

These structures were validated with the MolProbity server.[38] Refinement statistics (Table I) reflected a well refined, high quality geometric

structure with 96.3% of residues located in the most favored regions of a Ramachandran plot, 99.6% in generally allowed regions and only 0.4% in disallowed regions. Residues located in disallowed regions in our structures were found within similar regions in many other GAPDH structures.[19–21]

Water molecules were added to the present models with Coot. The peak contoured at 1.8σ in 2Fo–Fc maps was identified as a water molecule. These were positioned only when well-defined positive peaks were evident in both 2Fo–Fc and Fo–Fc electron density maps and when they could form a hydrogen bond(s) with either protein atoms or other water molecules.

Structural analyses

The programs Coot, Chimera,[39,40] and PyMol (vision 1.5.0, The PyMol Molecular Graphics System, Schrodinger, LLC.) were used for structural analyses. Structure refinement was performed with Coot. Superimposition of structures and RMSD calculations were performed with Chimera. Structural visualization and analyses were performed with Chimera and PyMol. Unless otherwise specified, structure figures were prepared using Chimera.

Acknowledgments

The authors thank Mrs. Susan Farr and Satsumi Roos for assistance with ROS preparation; Drs. Philip Kiser and David Lodowski for helping with data collecting and processing; Dr. Prem Kaushal for helping with structure refinement; Dr. Leslie T. Webster, Jr. for valuable comments on the manuscript. Synchrotron data collections were conducted at the Advanced Photon Source on the Northeastern Collaborative Access Team beamlines, as well as at the National Synchrotron Light Source on the X29 beamlines, which is operated by the Case Center for Synchrotron Biosciences. K.P. is John H. Hord Professor of Pharmacology.

References

1. Seidler NW (2013) Basic biology of GAPDH. Adv Exp Med Biol 985:1–36.
2. Sirover MA (1999) New insights into an old protein: the functional diversity of mammalian glyceraldehyde-3-phosphate dehydrogenase. Biochim Biophys Acta 1432:159–184.
3. Sirover MA (2011) On the functional diversity of glyceraldehyde-3-phosphate dehydrogenase: biochemical mechanisms and regulatory control. Biochim Biophys Acta 1810:741–751.
4. Padgett CM, Whorton AR (1995) *S*-nitrosoglutathione reversibly inhibits GAPDH by *S*-nitrosylation. Am J Physiol 269:C739–C749.
5. Mohr S, Stamler JS, Brune B (1996) Posttranslational modification of glyceraldehyde-3-phosphate dehydrogenase by *S*-nitrosylation and subsequent NADH attachment. J Biol Chem 271:4209–4214.
6. Hara MR, Cascio MB, Sawa A (2006) GAPDH as a sensor of NO stress. Biochim Biophys Acta 1762:502–509.
7. Hara MR, Snyder SH (2006) Nitric oxide-GAPDH-Siah: a novel cell death cascade. Cell Mol Neurobiol 26:527–538.
8. Sato M, Ohtsuka T, Stell WK (2011) Endogenous nitric oxide enhances the light-response of cones during light-adaptation in the rat retina. Vision Res 51:131–137.
9. Ko ML, Shi L, Huang CC, Grushin K, Park SY, Ko GY (2013) Circadian phase-dependent effect of nitric oxide on L-type voltage-gated calcium channels in avian cone photoreceptors. J Neurochem 127:314–328.
10. Chakravarti R, Aulak KS, Fox PL, Stuehr DJ (2010) GAPDH regulates cellular heme insertion into inducible nitric oxide synthase. Proc Natl Acad Sci USA 107: 18004–18009.
11. Hannibal L, Collins D, Brassard J, Chakravarti R, Vempati R, Dorlet P, Santolini J, Dawson JH, Stuehr DJ (2012) Heme binding properties of glyceraldehyde-3-phosphate dehydrogenase. Biochemistry 51:8514–8529.
12. Kwok MC, Holopainen JM, Molday LL, Foster LJ, Molday RS (2008) Proteomics of photoreceptor outer segments identifies a subset of SNARE and Rab proteins implicated in membrane vesicle trafficking and fusion. Mol Cell Proteomics 7:1053–1066.
13. Brownlee M (2005) The pathobiology of diabetic complications: a unifying mechanism. Diabetes 54:1615–1625.
14. Du Y, Miller CM, Kern TS (2003) Hyperglycemia increases mitochondrial superoxide in retina and retinal cells. Free Radic Biol Med 35:1491–1499.
15. Madsen-Bouterse S, Mohammad G, Kowluru RA (2010) Glyceraldehyde-3-phosphate dehydrogenase in retinal microvasculature: implications for the development and progression of diabetic retinopathy. Invest Ophthalmol Vis Sci 51:1765–1772.
16. Blatnik M, Frizzell N, Thorpe SR, Baynes JW (2008) Inactivation of glyceraldehyde-3-phosphate dehydrogenase by fumarate in diabetes: formation of *S*-(2-succinyl)cysteine, a novel chemical modification of protein and possible biomarker of mitochondrial stress. Diabetes 57:41–49.
17. Kowluru RA, Atasi L, Ho YS (2006) Role of mitochondrial superoxide dismutase in the development of diabetic retinopathy. Invest Ophthalmol Vis Sci 47:1594–1599.
18. Chiu CJ, Taylor A (2011) Dietary hyperglycemia, glycemic index and metabolic retinal diseases. Prog Retin Eye Res 30:18–53.
19. Ismail SA, Park HW (2005) Structural analysis of human liver glyceraldehyde-3-phosphate dehydrogenase. Acta Crystallogr D 61:1508–1513.
20. Frayne J, Taylor A, Cameron G, Hadfield AT (2009) Structure of insoluble rat sperm glyceraldehyde-3-phosphate dehydrogenase (GAPDH) via heterotetramer formation with Escherichia coli GAPDH reveals target for contraceptive design. J Biol Chem 284:22703–22712.
21. Jenkins JL, Tanner JJ (2006) High-resolution structure of human D-glyceraldehyde-3-phosphate dehydrogenase. Acta Crystallogr D 62:290–301.
22. Cowan-Jacob SW, Kaufmann M, Anselmo AN, Stark W, Grutter MG (2003) Structure of rabbit-muscle glyceraldehyde-3-phosphate dehydrogenase. Acta Crystallogr D 59:2218–2227.
23. Kuzminskaya EV, Asryants RA, Nagradova NK (1992) Rabbit muscle D-glyceraldehyde-3-phosphate dehydrogenase: half-of-the-sites reactivity of the enzyme

modified at arginine residues. Biochem Biophys Res Commun 187:577–583.
24. Hsu SC, Molday RS (1990) Glyceraldehyde-3-phosphate dehydrogenase is a major protein associated with the plasma membrane of retinal photoreceptor outer segments. J Biol Chem 265:13308–13313.
25. Ramachandran GN, Ramakrishnan C, Sasisekharan V (1963) Stereochemistry of polypeptide chain configurations. J Mol Biol 7:95–99.
26. Buehner M, Ford GC, Moras D, Olsen KW, Rossmann MG (1974) Structure determination of crystalline lobster D-glyceraldehyde-3-phosphate dehydrogenase. J Mol Biol 82:563–585.
27. Rao ST, Rossmann MG (1973) Comparison of supersecondary structures in proteins. J Mol Biol 76:241–256.
28. Talfournier F, Colloc'h N, Mornon JP, Branlant G (1999) Functional characterization of the phosphorylating D-glyceraldehyde 3-phosphate dehydrogenase from the archaeon *Methanothermus fervidus* by comparative molecular modelling and site-directed mutagenesis. Eur J Biochem 265:93–104.
29. Duee E, Olivier-Deyris L, Fanchon E, Corbier C, Branlant G, Dideberg O (1996) Comparison of the structures of wild-type and a N313T mutant of *Escherichia coli* glyceraldehyde 3-phosphate dehydrogenases: implication for NAD binding and cooperativity. J Mol Biol 257:814–838.
30. Roitel O, Vachette P, Azza S, Branlant G (2003) P but not R-axis interface is involved in cooperative binding of NAD on tetrameric phosphorylating glyceraldehyde-3-phosphate dehydrogenase from *Bacillus stearothermophilus*. J Mol Biol 326:1513–1522.
31. Tien YC, Chuankhayan P, Huang YC, Chen CD, Alikhajeh J, Chang SL, Chen CJ (2012) Crystal structures of rice (*Oryza sativa*) glyceraldehyde-3-phosphate dehydrogenase complexes with NAD and sulfate suggest involvement of Phe37 in NAD binding for catalysis. Plant Mol Biol 80:389–403.
32. Talfournier F, Colloc'h N, Mornon JP, Branlant G (1998) Comparative study of the catalytic domain of phosphorylating glyceraldehyde-3-phosphate dehydrogenases from bacteria and archaea via essential cysteine probes and site-directed mutagenesis. Eur J Biochem 252:447–457.
33. Otwinowski Z, Minor W (1997) Processing of X-ray diffraction data collected in oscillation mode. Macromol Cryst A 276:307–326.
34. McCoy AJ, Grosse-Kunstleve RW, Adams PD, Winn MD, Storoni LC, Read RJ (2007) Phaser crystallographic software. J Appl Cryst 40:658–674.
35. Winn MD, Ballard CC, Cowtan KD, Dodson EJ, Emsley P, Evans PR, Keegan RM, Krissinel EB, Leslie AG, McCoy A, McNicholas SJ, Murshudov GN, Pannu NS, Potterton EA, Powell HR, Read RJ, Vagin A, Wilson KS (2011) Overview of the CCP4 suite and current developments. Acta Crystallogr D 67:235–242.
36. Vagin AA, Steiner RA, Lebedev AA, Potterton L, McNicholas S, Long F, Murshudov GN (2004) REFMAC5 dictionary: organization of prior chemical knowledge and guidelines for its use. Acta Crystallogr D 60:2184–2195.
37. Emsley P, Cowtan K (2004) Coot: model-building tools for molecular graphics. Acta Crystallogr D 60:2126–2132.
38. Chen VB, Arendall WB 3rd, Headd JJ, Keedy DA, Immormino RM, Kapral GF, Murray LW, Richardson JS, Richardson DC (2010) MolProbity: all-atom structure validation for macromolecular crystallography. Acta Crystallogr D 66:12–21.
39. Goddard TD, Huang CC, Ferrin TE (2007) Visualizing density maps with UCSF chimera. J Struct Biol 157: 281–287.
40. Yang Z, Lasker K, Schneidman-Duhovny D, Webb B, Huang CC, Pettersen EF, Goddard TD, Meng EC, Sali, A, Ferrin TE (2012) UCSF chimera, MODELLER, and IMP: an integrated modeling system. J Struct Biol 179: 269–278.